TECHNICAL MEMORANDUM
X-352

THE AERODYNAMIC-FORCE AND HEAT-TRANSFER CHARACTERISTICS

OF LIFTING REENTRY BODIES

By William O. Armstrong, P. Calvin Stainback,
and Charles H. McLellan

Langley Research Center
Langley Field, Va.

FACILITY FORM 602

(ACCESSION NUMBER) N71 75470 (THRU)

23
(PAGES)

None
(CODE)

(NASA CR OR TMX OR AD NUMBER)

(CATEGORY)

NATIONAL AERONAUTICS AND SPACE ADMINISTRATION

WASHINGTON   August 1960

NATIONAL AERONAUTICS AND SPACE ADMINISTRATION

TECHNICAL MEMORANDUM X-352

THE AERODYNAMIC-FORCE AND HEAT-TRANSFER CHARACTERISTICS

OF LIFTING REENTRY BODIES*

By William O. Armstrong, P. Calvin Stainback,
and Charles H. McLellan

SUMMARY

An extensive investigation is in progress to study the aerodynamic-force and heat-transfer characteristics of a large number of lifting-body shapes of varying geometry. This study indicates that in many ways body shape is of secondary importance to other design parameters such as size, weight, planform loading, and lift-drag ratio. Furthermore, for given ratios of lift to drag and weight to base area no specific body shape was found to possess sufficiently superior qualities to exclude consideration of other body shapes. However, the configurations with more nearly flat bottoms appeared to offer some advantages from the standpoint of performance and heat-transfer considerations. Further studies are needed especially to develop more adequate methods of heat-transfer analysis for the more complex configurations.

INTRODUCTION

At the present time, the reentry requirements of space vehicles are not clearly defined and values of maximum lift-drag ratio from 0 to about 2 must be considered. The configurations with high lift-drag ratios provide the largest amount of maneuverability and the greatest reduction in reentry deceleration, while the shapes with low lift-drag ratio have the advantage of a lower total heat load. Since a wide variety of configurations are capable of providing a given lift-drag ratio in the range up to about 2, an extensive investigation is in progress to study the aerodynamic characteristics of a wide variety of generalized lifting-body shapes of varying geometry.

A series of lifting-body configurations shown in figures 1 and 2 have been studied and include full cones, round-bottom half cones and half elliptical cones, flat-bottom half cones of varying types and

amounts of bluntness, segmented conical bodies, and configurations with triangular cross sections. The aerodynamics of all of these configurations have not been examined in detail for the present investigation, but rather a broad view of the overall results has been taken to isolate the significant differences among classes of configurations. If comparisons are restricted to body shapes of the same design maximum lift-drag ratio and the same internal stowage capacity, many of these configurations have rather similar aerodynamic and heat-transfer characteristics. However, a few shape families were found to have important differences in their force and heating characteristics. One shape parameter for which these differences were significant was the curvature of the lifting surface of the vehicle - shown by such configurations as the round- and flat-bottom half-cone body shapes. This paper will discuss at some length the effects of this variation on the force and heat-transfer characteristics of these body shapes. Longitudinal force and stability data, however, have been obtained for all of these configurations, and directional stability and control data were obtained for a few of the more typical configurations.

SYMBOLS

A   maximum body cross-sectional area

a   semiminor axis of ellipse

b   semimajor axis of ellipse

C_D drag coefficient, Drag/qA

C_L lift coefficient, Lift/qA

C_{L_α} lift-curve slope at $\alpha = 0^\circ$, $\partial C_L/\partial\alpha$

C_l rolling-moment coefficient, $\text{Rolling moment}/qAD$

C_{l_β} rolling-moment derivative, $\partial C_l/\partial\beta$

C_m pitching-moment coefficient, $\text{Pitching moment}/qAD$

C_{m_α} longitudinal-stability derivative, $\partial C_m/\partial\alpha$

C_n yawing-moment coefficient, $\text{Yawing moment}/qAD$

C_{n_β} directional-stability derivative, $\partial C_n/\partial \beta$

D   maximum body diameter

h   body height at juncture of nose and afterbody

L/D   lift-drag ratio, C_L/C_D

M   Mach number

N_{Re} free-stream Reynolds number

q   free-stream dynamic pressure

R   maximum body radius

r   radius of blunted nose cap

S   surface area

s   distance along the body surface

T   temperature

W   weight

W/S   body planform loading

α angle of attack

β angle of sideslip

δ deflection angle

θ body semiapex angle

ϕ body radial angle

Subscripts:

f   flaps

MAX   maximum

n   nose

p   planform

L-1043

DISCUSSION

Force and Moment Study

Most of the test results were obtained at a Mach number of 9.6 in air, but in order to assess the effect of Mach number variation, several configurations were tested for a range of Mach numbers from about 3 to 18. Results for two of these configurations are shown in figure 3 which presents the variation of $(L/D)_{MAX}$, C_{L_α}, C_{m_α}, and C_{n_β} with Mach number for a round-bottom configuration with a spherically blunted nose and a flat-bottom configuration with a canted flat face. All tests were made at a N_{Re} (based on body diameter) of 0.2 million except where noted. This Reynolds number should be representative of flight values for a reasonably sized vehicle at a Mach number of about 20. Data presented for Mach numbers above 10 were obtained in helium.

Newtonian estimates (where pressure ratio is equal to $2 \sin^2\delta$) were made for the round-bottom configuration, and predictions of $(L/D)_{MAX}$ including skin friction show good agreement with experiment, particularly in the hypersonic Mach number range. Since the drag of this low $(L/D)_{MAX}$ configuration is primarily wave drag, the inviscid $(L/D)_{MAX}$ would be only slightly higher than that shown in figure 3. Predictions of C_{L_α} were made by using a somewhat more sophisticated cone—flat-plate theory which combined the effects of the body upper surface estimated by shock-expansion theory with those of the body compression surfaces calculated by using cone data from reference 1 for the conic afterbody and the Newtonian theory for the spherically blunted nose. Figure 3 shows very good agreement between the predicted and experimental values of C_{L_α} throughout the Mach number range. Both experiment and theory approach the Newtonian values of C_{L_α} at the higher Mach numbers. The predicted values of the stability parameters for the round-bottom configuration also agree fairly well with those shown experimentally, and they exhibit the same trends in the high Mach number range. The moments about the moment-center location selected (centroid of the side-view area) are rather small and the variations in the experimental values of C_{m_α} in the hypersonic speed range represent less than a 2-percent change in the body aerodynamic-center position.

The important thing to note from figure 3, however, is that both experimental and predicted results show no appreciable variations in the aerodynamic characteristics of these configurations with Mach number in the higher hypersonic speed range; therefore, data for $M = 9.6$ would be expected to be representative of the aerodynamic characteristics in the high Mach number range for ideal-gas conditions. Unpublished

results from the Langley Research Center indicate that the real-gas effects would be small for bodies of this type.

As previously mentioned, a large variety of lifting bodies are capable of providing a given L/D in the range of interest for reentry. Effects of some of the variations in body configurations shown in the previous figures, such as nose bluntness, are fairly obvious; however, effects of other geometric changes such as varying body cross section may be less apparent. Some of these effects are shown in figure 4 in which $(L/D)_{MAX}$ is plotted against semiapex angle of the bodies.

Experimental results for the round- and flat-bottom shapes are shown by the solid and long-dashed lines, respectively. Newtonian predictions are also included for the sharp round-bottom and flat-bottom half cones. Flagged test-point symbols indicate body shapes having a nose-bluntness ratio h/R equal to 0.4. Figure 4 shows that even the blunter half-body shapes have $(L/D)_{MAX}$ values greater than 0.5. In fact, the half hemisphere has a predicted L/D of 0.5 with the flat surface parallel to the flow and L/D is shown experimentally to be about 0.43. On the other hand, relatively slender bodies are required if values of L/D of 1.5 or greater are desired. As predicted by the Newtonian theory, the flat-bottom half cones have a higher $(L/D)_{MAX}$ than the round-bottom ones. Experimental data also show the same characteristics for the triangular body sections. Increasing the cone semiapex angle is shown to reduce the difference in $(L/D)_{MAX}$ between the round-bottom and flat-bottom half-cone shapes. Eliminating the high-drag, low-lift sides of the sharp round-bottom half cones, as shown by the $\phi = 45^{O}$ conic segmented body shapes, increases the $(L/D)_{MAX}$ of the configuration; however, this increased $(L/D)_{MAX}$ is accompanied by a reduction in body volume.

For a given design $(L/D)_{MAX}$, the flat-bottom half-cone approach will obviously permit the use of a blunter vehicle which may have some advantages structurally. For example, if an $(L/D)_{MAX}$ of 1.3 is desired, a round-bottom half-cone body with 0.4 bluntness requires a half-cone angle of 10° for this $(L/D)_{MAX}$. However, the half-cone angle can be increased to about 18° for a flat-bottom configuration with the same bluntness and $(L/D)_{MAX}$.

It has been shown that there are differences in the $(L/D)_{MAX}$ of the flat-bottom and round-bottom half-cone configurations; therefore, it would be of interest to examine the longitudinal characteristics of a series of these types of configurations. Figures 5 and 6 present the variation in C_m with angle of attack for a series of round-bottom and flat-bottom cone configurations of varying bluntness. For this study, the moment reference center was arbitrarily chosen as the centroid of

the side-view area. Figure 5 presents test results for a series of round-bottom half-cone configurations for four bluntness ratios h/R of 0, 0.2, 0.4, and 0.6 and three semiapex angles of 10°, 20°, and 40°. Since reentry vehicles will operate primarily in the angle-of-attack range between $(L/D)_{MAX}$ and $C_{L,MAX}$ this angle-of-attack range will be of most interest.

Figure 5 shows that the addition of nose bluntness generates regions of instability in the moment data of the more slender bodies as seen by comparing the sharp 10° half cone with the 0.2 bluntness case. These regions of instability are dissipated by increasing nose bluntness or by increasing the cone semiapex angle. Qualitatively, theory indicates that these unstable regions are due to the interference effects of the blunt nose on the flow field of the body. Methods have not as yet been developed for making a quantitative analysis of the three-dimensional flow fields of these blunted bodies at angles of attack. The existence of these interference effects were clearly seen, however, in schlieren photographs of these tests. Although unstable regions such as these can undoubtedly be handled, they do introduce some additional stability problems which may require a penalty in center-of-gravity position or additional stabilizing surfaces.

Figure 6 shows that essentially the same regions of instability as previously noted for the round-bottom configuration are also found for the flat-bottom case as the configuration is blunted. Here, the nose was blunted by means of a flat canted face having 45°, 60°, and 90° of nose cant. Again, nose bluntness results in regions of instability similar to those shown for the round-bottom case as seen by comparing the sharp configuration with that having a 0.2 bluntness ratio.

These unstable regions are again shown to disappear with increasing nose bluntness. In fact, for the more highly canted faces ($\delta_n = 45^{\circ}$ and 60°) these unstable regions disappear somewhat more rapidly with increased bluntness than for the round-bottom case. Nose cant provides a sizable pitch-up moment for trimming the configuration at or above $C_{L,MAX}$ so that trailing-edge flaps can be used for trimming at lower angles of attack. The amount of cant required will depend on the actual design and its center-of-gravity location; however, the 60° face cant appears adequate for the center-of-gravity position of the present discussion. It should also be mentioned that variation in cant angle had no appreciable effect on the value of either $(L/D)_{MAX}$ or $C_{L,MAX}$ or the angle of attack at which they occurred for bluntnesses up to about 0.4.

Trim and directional stability coefficients are also important in discussing the aerodynamic characteristics of these lifting-body configurations. While it is impractical to obtain trim and directional data for all of the configurations tested, a few representative models

of both the configurations with relatively low L/D (L/D ≈ 0.5) and the shapes with relatively high L/D (L/D ≈ 1.5) were tested. Figure 7 shows the trim characteristics of three configurations having a value of $(L/D)_{MAX}$ of around 0.6 or 0.7. Similar results for the configurations with higher L/D are shown on figure 8. An arbitrary flap size equal to 10 percent of the body planform area was selected for all configurations. These figures present the variation of C_m with α for the various configurations trimmed at both $(L/D)_{MAX}$ and $C_{L,MAX}$.

The configurations with low $(L/D)_{MAX}$ shown in figure 7 consisted of a blunted flat-bottom, 10° semiapex-angle, half-cone body with a 60° canted flat face and two blunted round-bottom configurations - one having the same canted face as the flat-bottom shape and the other having a spherically blunted nose and a 30° semiapex-angle conic afterbody. The body shapes with higher $(L/D)_{MAX}$ shown in figure 8 consisted of round- and flat-bottom, 10° semiapex angle, half-cone bodies with a 0.3 bluntness ratio and a 60° canted flat face, and a 20° semiapex-angle quarter-conic segmented body with a spherically blunted nose. Again, the body center-of-gravity location was chosen as the centroid of the side-view area except for the case shown in figure 8 of the round-bottom half-cone configuration with a high $(L/D)_{MAX}$. For this body shape, a 1.4-percent rearward shift of the body center of gravity from the side-view area centroid was required in order to trim the configuration at angles of attack up to $C_{L,MAX}$.

Similar trends were observed in the trim characteristics of both the body shapes with low $(L/D)_{MAX}$ ($(L/D)_{MAX}$ ≈ 0.6 or 0.7 shown in fig. 7) and the configurations with higher $(L/D)_{MAX}$ ($(L/D)_{MAX}$ ≈ 1.5 shown in fig. 8). From these figures, it can be seen that all these configurations can be trimmed by means of the relatively simple afterbody flap having a flap area equal to 10 percent of the planform area and that they exhibit stable characteristics throughout the angle-of-attack range considered. Predicted moments are shown by the solid and dashed curves and were obtained by adding the incremental flap pitching moments predicted by Newtonian theory to the experimental value of the basic body. Good agreement is shown between these predictions and experimental data. Geometrically, the flat-bottom configuration lends itself to the use of a short, full-span flap and requires relatively low amounts of flap deflection for trim. It might also be mentioned that the trim values for $(L/D)_{MAX}$ and $C_{L,MAX}$ were only slightly different from those obtained for the untrimmed vehicles.

The directional and lateral characteristics of the two round- and flat-bottom half-cone bodies with a flat canted nose are shown in figures 9 and 10. Data for the bodies with low $(L/D)_{MAX}$ are presented in figure 9, and figure 10 presents data for the higher $(L/D)_{MAX}$ shapes.

These figures show the experimental variation in C_{n_β} and C_{l_β} with angle of attack and compare these experimental results with predicted values obtained by means of Newtonian theory. It may be seen from figures 9 and 10 that this theory gives reasonable predictions of the lateral and directional characteristics of the body shapes with both low and high $(L/D)_{MAX}$ and provides an excellent indication of the trends of the stability derivatives with angle of attack.

Here, as in the case of the trim characteristics, the configurations with both low and high $(L/D)_{MAX}$ exhibit similar trends in their lateral and directional characteristics. Both flat-bottom configurations are shown to have low positive values of directional stability and virtually no dihedral effects, particularly at the high angles of attack. Since the basic flat-bottom configurations possess a relatively small degree of inherent stability, some modifications would undoubtedly be needed to increase their stability. However, these low values of C_{n_β} and C_{l_β} need not necessarily constitute a serious stability problem, since there is a variety of body modifications possible to tailor the stability of the vehicle to the requirements of its particular mission.

An example of one possible modification is shown on figure 9 in which a side flap with span and chord equal to 0.2 of the body diameter was added to both the round- and flat-bottom body shapes of low $(L/D)_{MAX}$. For the flat-bottom case, the flap was rolled out 10° and attached along an extended line of the body surface. The same sized flap was also tested on the round-bottom configuration. In this case, the top of the flap was again rolled out 10° and was attached parallel to the body center line. Results from these tests, indicated by the square symbols on the figure, show that, while these flaps have little effect on the stability derivatives at $\alpha = 0^\circ$, both the lateral and directional stability of the vehicles are increased at angles of attack near 30° - the range of primary interest.

The round-bottom configurations were found to have a large amount of inherent directional stability along with large values of positive dihedral. These large values of roll due to sideslip are usually undesirable from a standpoint of dynamic stability.

L-1043

Heat-Transfer Study

Thus far, only a discussion of the force and moment characteristics of the configurations considered has been made. However, since the heating characteristics of these bodies are of equal importance, an analysis of these characteristics was made for a few of the configurations. The heat-transfer studies were limited to simple, basic shapes that were amenable to theoretical analysis which should give results with engineering accuracy. Only basic body shapes have been included in the heat-transfer investigation; therefore, the results do not represent the heating characteristics of complete vehicles, which can be altered by the addition of control and stabilizing surfaces. The following analysis will be subdivided into two parts and will consider the total heat absorbed and the peak heating rates encountered during entry.

First to be considered is the effect of body geometry and lift-drag ratio on the total heat load, a parameter of importance for heat sink and ablation shielding. In figure 11, the heat load is presented as a function of the lift-drag ratio for three types of half-body configurations entering the earth's atmosphere from a decaying orbit at zero angle of attack. The method for calculating these heating rates was taken from reference 2. The configurations considered are: (a) half cones of semicircular cross section having bluntness ratios, that is, the ratio of cap radius to base radius, of 0, 0.2, and 0.4, (b) half cones of semicircular cross section having flat nose section with a bluntness ratio h/R of 0.3, and (c) an 80° swept, 45° dihedral configuration.

Along each of the curves for these four configurations (fig. 11), the cone semiapex angle varies from 10° (high L/D) to 40° (low L/D) for the 0 and 0.2 curves and from 20° to 40° for the 0.3 and 0.4 curves.

The ordinate scale is the heat load for the configuration (neglecting the heating rate to the upper surface and the effects of radiation) nondimensionalized in terms of the heat load of a sphere of the same cross-sectional area and weight entering on a nonlifting trajectory. The heating rates in this figure and in the subsequent ones have been calculated from laminar-boundary-layer theory where possible or by engineering estimates when the shapes were too complex from a theoretical viewpoint. For example, the heat transfer to the blunted cones was calculated from the laminar-boundary-layer theory of reference 3 by assuming that the absence of the upper surface had no influence on the heat-transfer rate to the remainder of the cone. The heat-transfer rate to the cone having a flat nose section was calculated in the same manner by assuming that flow originated at the virtual tip of the blunted cone. The average heat transfer to the flat nose section was assumed to be equal to that of a circular flat face having an area equal to that of the cone face. The average heat-transfer rate for the circular flat face was assumed to be

1.1 times the stagnation-point value. The stagnation-point heat-transfer rate was assumed to be 0.575 of the stagnation-point value of a hemispherically blunted body of equal radius. The heat-transfer rate to the 80° swept, 45° dihedral configuration was estimated by calculating the average heat-transfer rate to an equivalent cone; that is, the cone and dihedral configuration were assumed to have equal surface pressures and lengths. This average heat-transfer rate was assumed to represent the average heating rate to the dihedral configuration; the total heat-transfer rate to this configuration was obtained from the assumed average heat-transfer rate and the area of the dihedral configuration.

Experimental lift-drag ratios, obtained from the force investigation, were used in all cases except for the Newtonian curve. The Newtonian curve was calculated for the hemispherically blunted body assuming inviscid flow and applies for all bluntness ratios from 0 to 1 and semi-apex angles from 10° to 40°.

The major point to note in this comparison is the predominant effect of lift-drag ratio on total heat load. In the region in which Newtonian theory predicted the lift and drag characteristics, the effect of body shape on heat load is important only insofar as the shape changes the value of L/D. Furthermore, in this same region, the assumption of Newtonian flow appears to give a useful, lower asymptotic value of the heat load.

Although figure 11 indicates that the effect of body shape on heat load is, in general, secondary to lift-drag-ratio effects, a somewhat more detailed analysis of the influence of body shape on heat load for a class of bodies previously discussed in the force-study section will be made. A comparison of the heat load for round-bottom and flat-bottom half-circular cones having fixed base areas and weights is presented in figure 12. In this figure, variations in L/D correspond to angle-of-attack changes in the high-drag portion of the lift-drag curve. The two solid curves are for the round-bottom configuration; the dashed curves are for the flat-bottom configuration.

For both configurations, the heat-transfer rate in the range of low L/D (i.e., high angle of attack) was calculated by assuming cross flow to exist over the body. The heat level to the most windward generator of the round-bottom cone was assumed to vary as the sine of the angle of attack of the cone center line as suggested in reference 4. For the flat-bottom cones at low angles of attack, the heat-transfer rate was calculated from strip theory. The two heating rates represented by the circular symbols on the curves for the round-bottom cones are for zero angle of attack and were taken from figure 11. The curves representing the heat load between the limits of these calculations were simply faired, and this faired region is indicated by the dotted section of the curves.

It should be noted that this comparison applies only for simple half-cone bodies, and configuration changes required to obtain vehicles with suitable aerodynamic characteristics must be considered in the final analysis of the total heat load. The heating to the upper surfaces of the configurations has been neglected in computing the heat load. This omission should not be serious, however, since a major portion of the curves for the flat-bottom configuration, where this omission could be serious, was computed for angles of attack equal to or greater than the cone semiapex angle.

Figure 12 indicates that for a given cone angle and L/D, the heat load of the flat-bottom configuration is less than that for the round-bottom configuration. Further, it appears that for low L/D operation, it is preferable, in general, to use a configuration with a low maximum L/D such as a 40° half cone in preference to a high L/D configuration such as a 20° half cone operating at very high angles of attack and, consequently, low values of L/D.

In the previous section, face cant was shown to provide desirable pitch-up moment for trim. The influence of nose-cant blunting on total heat load will be discussed in a limited way. In figure 13 the curve represents the heat load for a 10° flat-bottom sharp half-circular cone. The two vertical lines represent the range of the heating estimate for the cone blunted by means of a flat face having a 60° cant. Bluntness ratios of 0.3 and 0.6 have been considered. The angle of attack of the blunted cone is 30°. The heat load for the blunt cones was calculated by three different procedures which are represented by the solid dots on the vertical line. The upper and lower dots represent the heat load calculated from strip theory. The lower dots represent the heating rate estimate made by assuming flow to start at the virtual tip of the cone; the calculations represented by the upper dots assumed that flow started at the physical leading edge. The middle dots and the curve for the 10° sharp half cone represent the heat estimate made by assuming cross flow. The lower two estimates probably more nearly indicate the change in the heat load due to bluntness while the upper points provide a conservatively high upper limit.

While the results are not conclusive, there appears to be, for these conditions, no significant effect of this type of nose blunting on the heat load for bluntness ratios of 0.3 and only a small penalty at a value of 0.6.

So far, the discussion has dealt only with the total heat loads of these various body shapes. Peak heating rate is an equally important design heating parameter which serves to indicate, to some degree, regions of the body structure requiring heat absorbing material as well as regions where a radiation-cooled structure might be used.

If the round- and flat-bottom body shapes of the same size and weight operating at a fixed L/D are again compared, two factors are found which influence heating rates over these bodies. These two factors are geometry (shape and vehicle attitude) and the difference in C_L at which these bodies operate for a given L/D which results in a difference in flight environment for the two body shapes.

Figures 14 and 15 show the total effect of these two factors, geometry and velocity-altitude differences, on the laminar peak heating rates for equilibrium flight at the body lower meridian or center line of these two vehicles. It should be noted that these heating rates are representative of those occurring over the major portion of the lifting surfaces; however, they do not take into account the edges of either of these bodies which are subjected to higher localized heating. Since in the force investigation bodies in two L/D ranges (about 0.7 and 1.4) have been considered, the distributions presented in figures 14 and 15 are for bodies of these L/D ranges. The peak heating rates in these figures are plotted as a function of distance along the body nondimensionalized in terms of the base radius.

Figure 14 shows that for configurations with both low and high L/D, the flat-bottom shapes, indicated by the dashed line, have a lower heating rate than the round-bottom shapes, shown by the solid curves. For the 40° half-cone shape operating at $L/D = 0.7$, the difference in the heating rate between the round- and flat-bottom configurations is primarily due to difference in body geometry since relatively small differences occurred in the trajectories of the two configurations. However, for the more slender 20° half-cone bodies operating at L/D of 1.4, both geometry and differences in C_L combine to lower the heating rates on the flat-bottom configuration.

Figure 15 shows the effect of nose bluntness on the peak heating rates of both the 40° and approximately 23° round-bottom half-cone shapes at zero angle of attack. Note that for this case the origin of the s/R coordinate is the tangency point of the spherical cap and the conical afterbody. In the case of the 40° cone it can be seen that while bluntness has little effect on the L/D of the configurations, the peak heating rate over the forebody is considerably reduced by increasing nose bluntness, whereas heating rate near the rear of the bodies is essentially unaffected by bluntness. This reduction in heating rate is essentially due to variation in body shape since the trajectories are the same for all configurations. Similar trends due to bluntness are also shown on the right for the more slender configurations with higher values of L/D.

These comparisons of body shape effects on the peak heating rate are independent of vehicle size and weight; however, the actual heating

rates of a configuration are of course strongly dependent upon these parameters. The heating rates shown on these figures are for an assumed weight-to-base-area ratio of 120 lb/sq ft and a base radius of 2.8 feet. This value of 120 lb/sq ft corresponds to a planform loading of about 70 lb/sq ft for a 20° cone and about 160 lb/sq ft for a 40° cone and these values are representative of lifting bodies currently being considered. The temperature scale is for radiation equilibrium and an assumed emissivity of 0.8. This temperature scale serves to indicate the surface temperature level associated with these bodies during equilibrium flight from a decaying orbit.

<div style="text-align:left">L
1
0
4
3</div>

CONCLUDING REMARKS

This investigation has served to point out some of the relative merits of several simple lifting-body configurations and indicates that in many ways body shape is of secondary importance to other design parameters such as size, weight, planform loading, and lift-drag ratio. Furthermore, for a given lift-drag ratio and weight-to-base-area ratio, no specific body shape was found to possess sufficiently superior qualities to exclude consideration of other body shapes. However, the configurations with more nearly flat bottoms appeared to offer some advantages from the standpoint of performance and heat-transfer considerations. Further studies are needed, especially to develop more adequate methods of heat-transfer analysis for the more complex configurations.

Langley Research Center,
      National Aeronautics and Space Administration,
            Langley Field, Va., April 11, 1960.

REFERENCES

1. Ames Research Staff: Equations, Tables, and Charts for Compressible Flow. NACA Rep. 1135, 1953. (Supersedes NACA TN 1428.)

2. Chapman, Dean R.: An Approximate Analytical Method for Studying Entry Into Planetary Atmospheres. NASA TR R-11, 1959. (Supersedes NACA TN 4276.)

3. Lees, Lester: Laminar Heat Transfer Over Blunt-Nosed Bodies at Hypersonic Flight Speeds. Jet Propulsion, vol. 26, no. 4, Apr. 1956, pp. 259-269.

4. Reshotko, Eli: Laminar Boundary Layer With Heat Transfer on a Cone at Angle of Attack in a Supersonic Stream. NACA TN 4152, 1957.

L
1
O
4
3
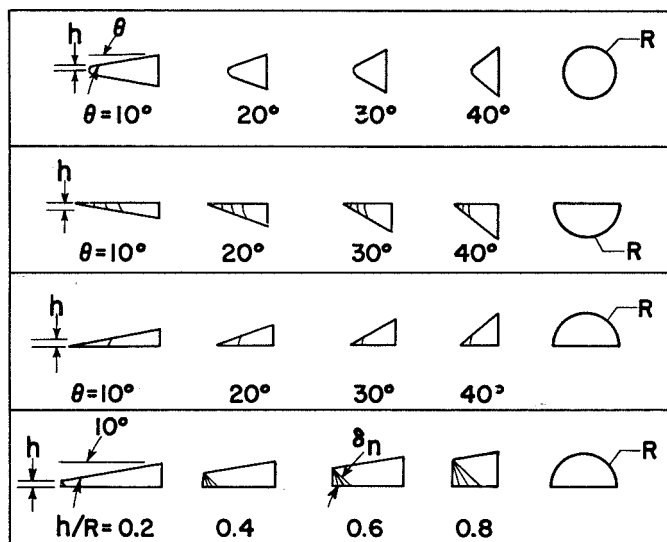
LIFTING BODIES

Figure 1

LIFTING BODIES

Figure 2

EFFECTS OF MACH NUMBER

Figure 3

EFFECTS OF CROSS SECTION ON $(L/D)_{MAX}$

M = 9.6

Figure 4

VARIATIONS IN c_m WITH NOSE BLUNTNESS

M=9.6

θ, DEG
10
20
40

$\frac{h}{R}=0$

$\frac{h}{R}=0.2$

$\frac{h}{R}=0.4$

$\frac{h}{R}=0.6$

α, DEG

α, DEG

Figure 5

VARIATIONS IN c_m WITH NOSE BLUNTNESS

M=9.6, 10° HALF-CONE

δ_n, DEG
45
60
90

$\frac{h}{R}=0$

$\frac{h}{R}=0.2$

h/R = 0.4

h/R = 0.6

α, DEG

α, DEG
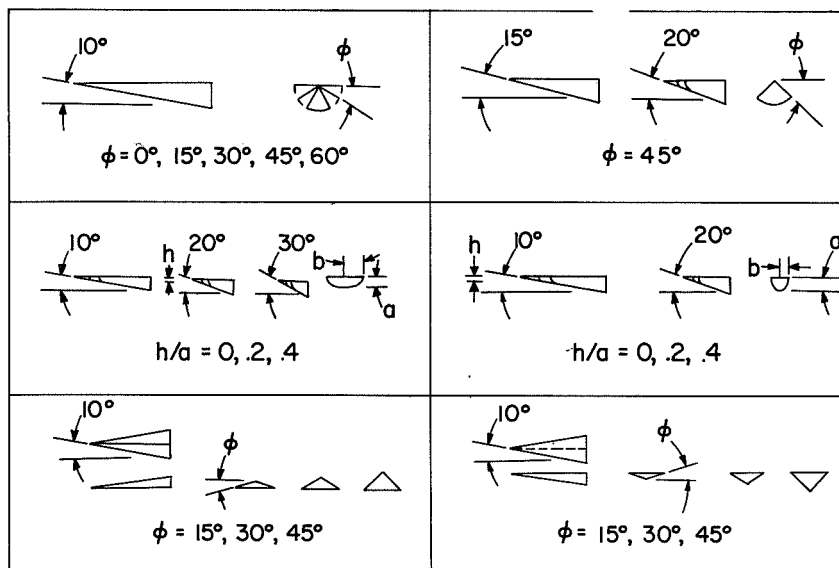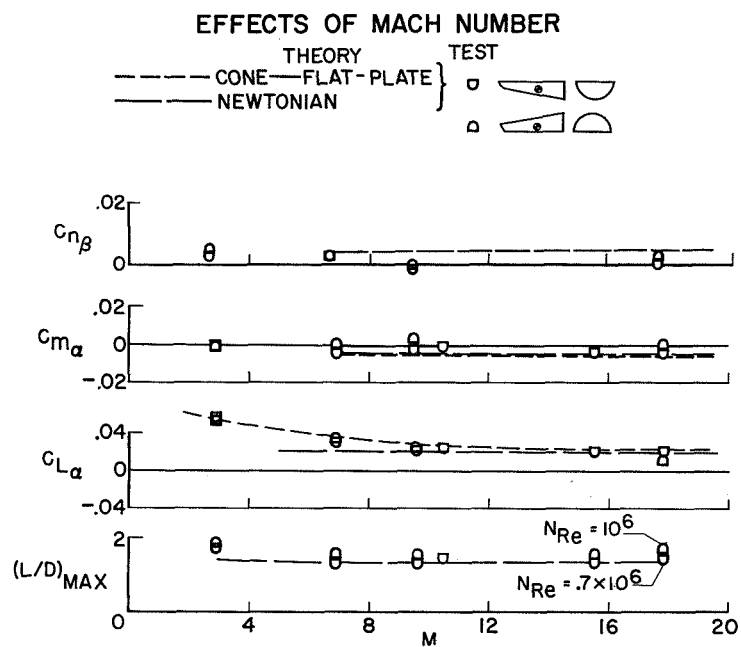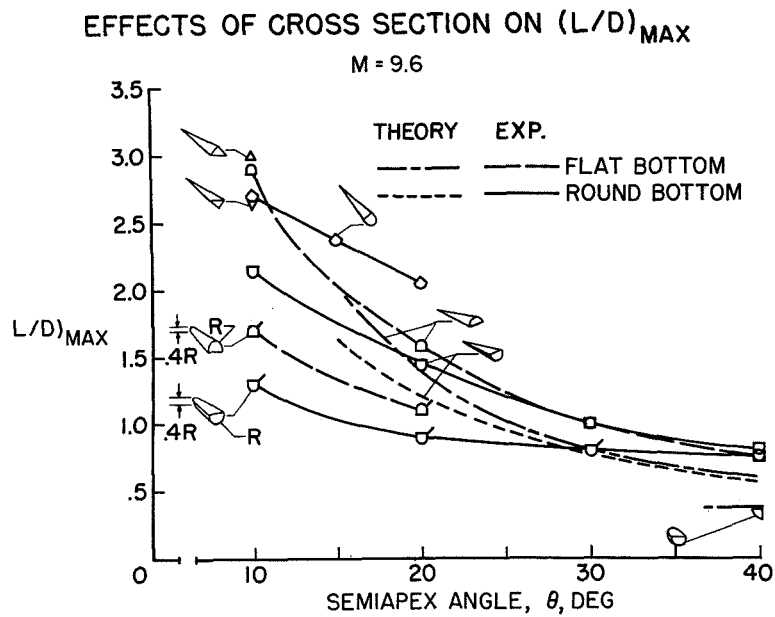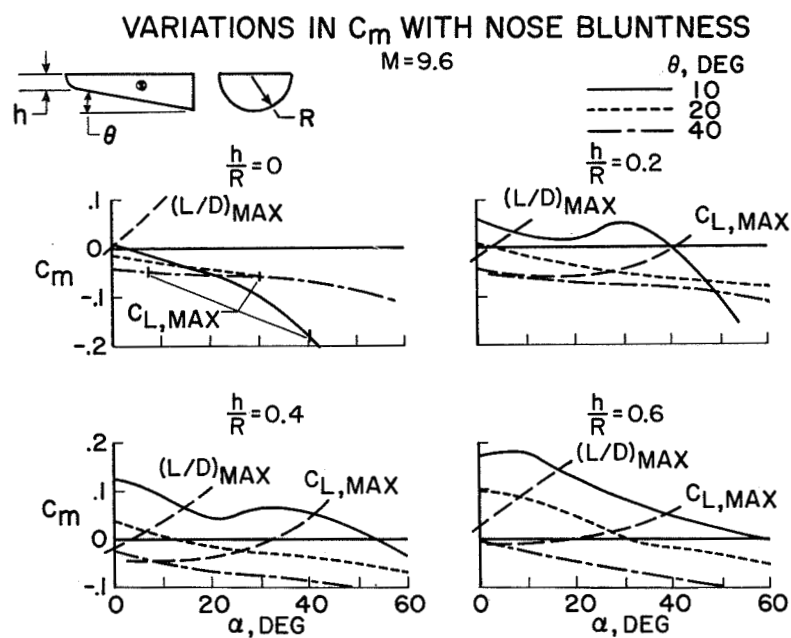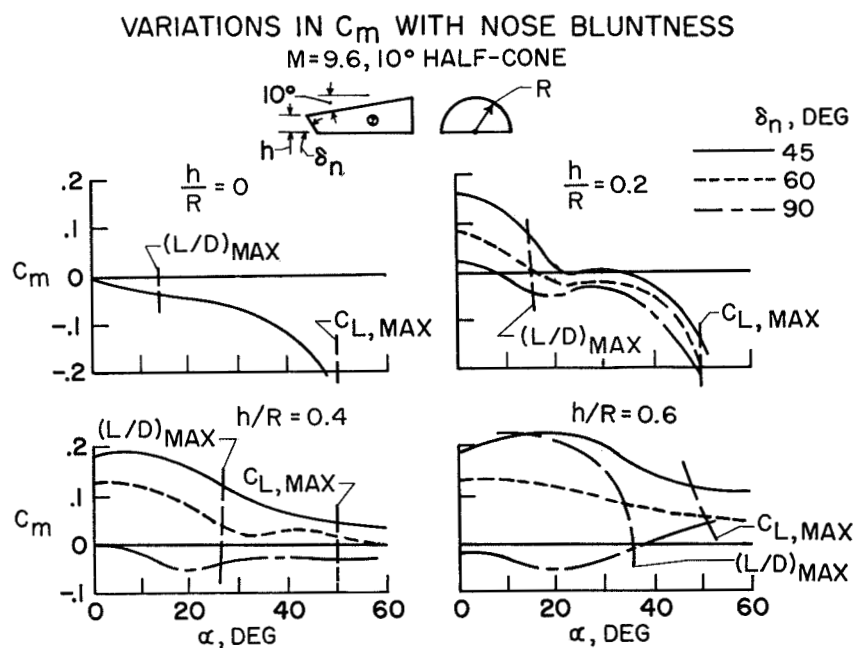
Figure 6

TRIM CHARACTERISTICS

$$\frac{S_f}{S_p} = 0.1; \quad M = 9.6; \quad (L/D)_{MAX} \approx 0.5$$

THEORY   TEST
———   o $(L/D)_{MAX,\ TRIM}$
------   □ $(C_{L,\ MAX})_{TRIM}$

.6R, 60°, 10° δ_f, R, .52R

$(L/D)_{MAX} = 0.73$
$C_{L,\ MAX} = 1.15$
$\delta_f = 23°$
$\delta_f = -3°$
C_m 0, .2, -.2
α, DEG, 0 20 40 60

.6R, 10°, R, 60° δ_f

$C_{L,\ MAX} = 1.45$
$\delta_f = -5°$
$\delta_f = 10°$
$(L/D)_{MAX} = 0.66$
C_m 0, .2, -.2
α, DEG, 0 20 40 60

.6R, 30° δ_f, R, .52R

$(L/D)_{MAX} = 0.59$
$C_{L,\ MAX} = 0.51$
$\delta_f = 23°$
$\delta_f = 54°$
C_m 0, .05, -.05
α, DEG, 0 20 40 60
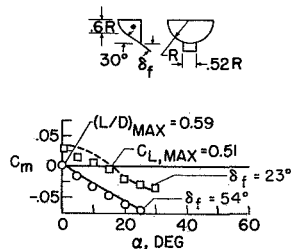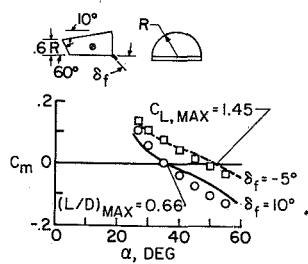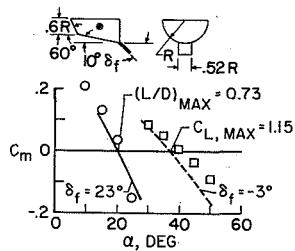
Figure 7

TRIM CHARACTERISTICS

$$\frac{S_f}{S_p} = .1; \quad M = 9.6; \quad (L/D)_{MAX} \approx 1.5$$

THEORY   TEST
———   o $(L/D)_{MAX,\ TRIM}$
------   □ $(C_{L,\ MAX})\ TRIM$

.3 R, 60°, 10°, R, .52 R

$(L/D)_{MAX} = 1.40$
$C_{L,\ MAX} = 1.51$
$\delta_f = 10°$
$\delta_f = -40°$
C_m 0, .1, -.1
α, DEG, 0 20 40 60

.3 R, 10°, R, 60° δ_f

$(L/D)_{MAX} = 1.48$
$C_{L,\ MAX} = 2.19$
$\delta_f = -10°$
NO FLAP
C_m 0, -.1, .1
α, DEG, 0 20 40 60

.4 R, .52 R, 20° δ_f, 45°, R

$(L/D)_{MAX} = 1.36$
$C_{L,\ MAX} = 1.36$
$\delta_f = 23°$
$\delta_f = 20°$
C_m 0, .05, -.05
α, DEG, 0 20 40 60

Figure 8

L-1043
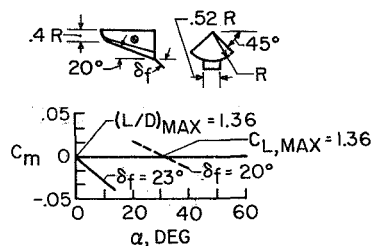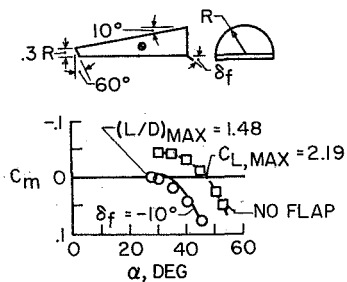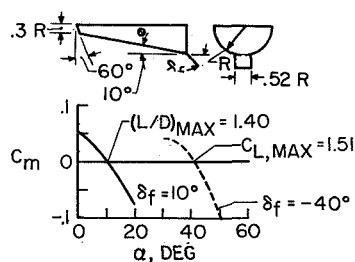
DIRECTIONAL STABILITY CHARACTERISTICS
$M = 9.6$; $(L/D)_{MAX} \approx 0.5$

- - - - NEWTONIAN THEORY
TEST
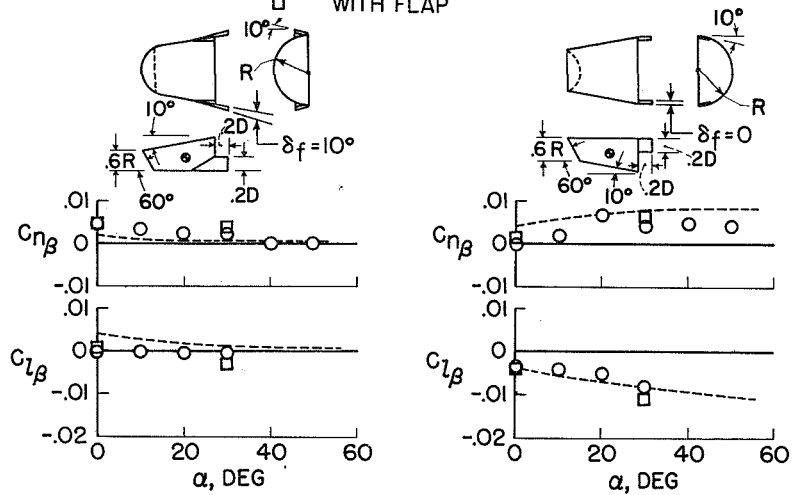O   WITHOUT FLAP
□   WITH FLAP

Figure 9

DIRECTIONAL STABILITY CHARACTERISTICS
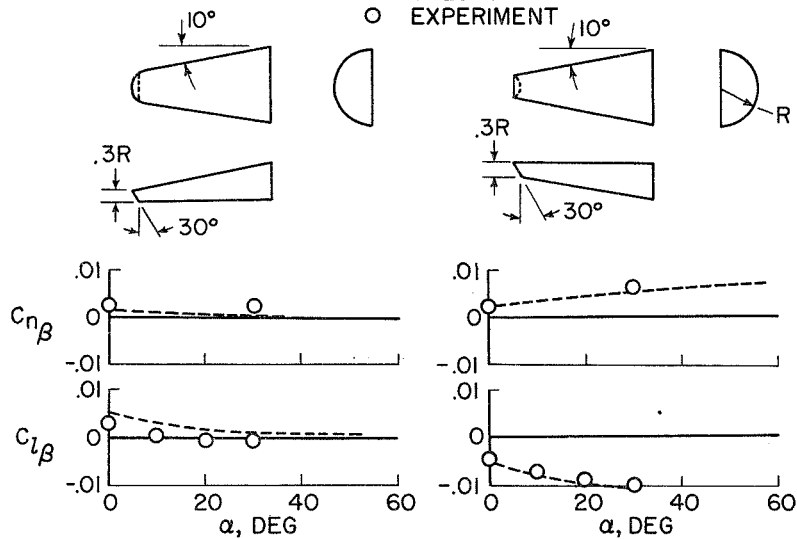### $M = 9.6$; $(L/D)_{MAX} \approx 1.5$

- - - - THEORY
O   EXPERIMENT

Figure 10

TRAJECTORY HEAT LOAD
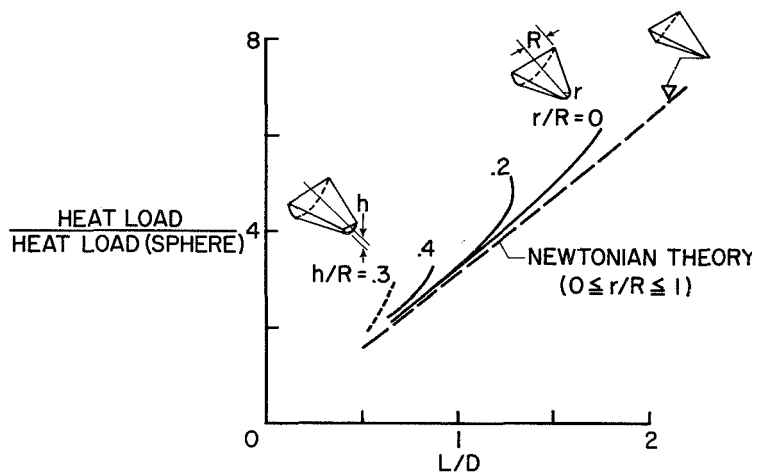
HALF–BODIES OF EQUAL WEIGHT AND BASE RADIUS; $\alpha = 0$

Figure 11

TRAJECTORY HEAT LOAD

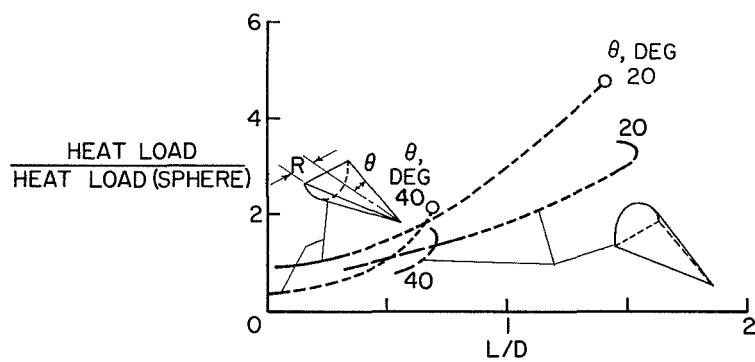HALF–CONES OF EQUAL WEIGHT AND BASE RADIUS; α = VARIABLE

Figure 12

TRAJECTORY HEAT LOAD FOR 10° HALF-CONE

60° CANTED FACE OF VARYING BLUNTNESS; α = VARIABLE
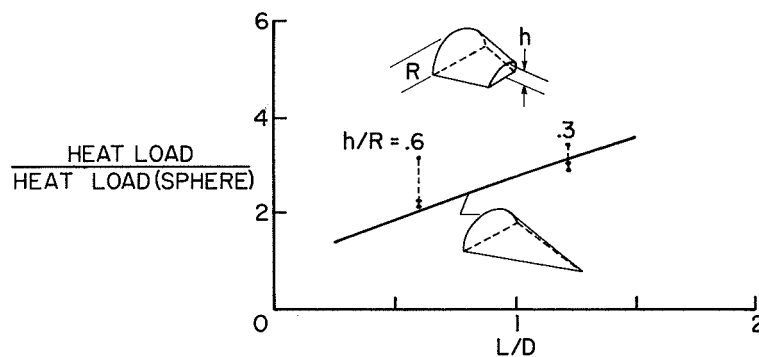
Figure 13

TRAJECTORY PEAK HEATING RATES

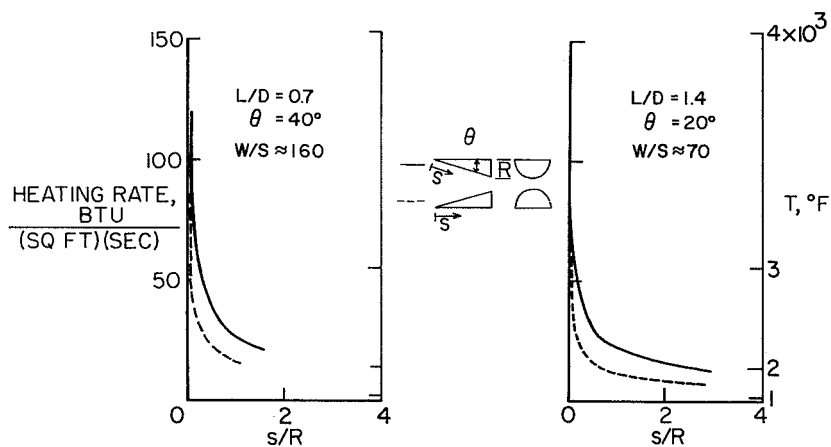ROUND- AND FLAT-BOTTOM HALF-CONES

W/A = 120 LB/SQ FT; R = 2.8 FT

Figure 14

TRAJECTORY PEAK HEATING RATES
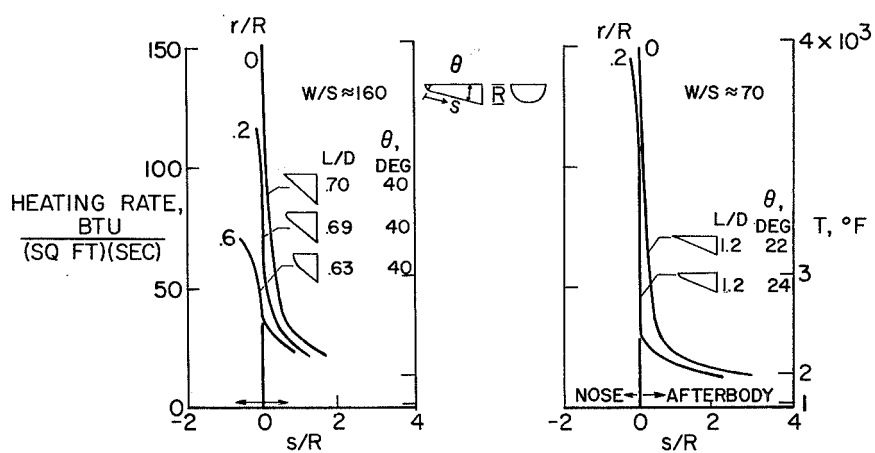NOSE BLUNTING; W/A=120 LB/SQ FT; R=2.8 FT; α = 0

Figure 15